Interdisciplinary Information Sciences, Vol. 13, No. 1, pp. 7–16 (2007)

Integrated Simulation of the Atomization Process of a Liquid Jet Through a Cylindrical Nozzle

Jun ISHIMOTO[1], Hidehiro HOSHINA[2], Tadashi TSUCHIYAMA[2], Hideyuki WATANABE[2], Asako HAGA[2] and Fuminori SATO[2]

[1]*Institute of Fluid Science, Tohoku University, 2-1-1, Katahira, Aoba-ku, Sendai 980-8577, Japan*
E-mail: ishimotojun@ieee.org
[2]*KEIHIN Co., Kakuda R & D Center, 197-1, Nagare, Kakuda, Kakuda 981-1505, Japan*

Received September 19, 2006; final version accepted January 22, 2007

The 3-D structure of liquid atomization behavior through a cylindrical nozzle is numerically investigated and visualized by a new type of integrated simulation technique. CFD (Computational Fluid Dynamics) analysis focused on the consecutive breakup of a liquid column, formation of liquid film, and generation of droplets of a cylindrical flow in the outlet section of the nozzle. Utilizing the governing equations for high-speed atomizing nozzle flow based on the LES-VOF model in conjunction with the CSF model, an integrated parallel computation is performed to clarify the detailed atomization process of a cylindrical nozzle flow and to acquire data, which is difficult to confirm by experiment, such as atomization length, liquid core shape, distribution droplet sizes, spray angle and droplet velocity profiles. According to the present analysis, the atomization rate and the droplets-gas two-phase flow characteristics are found to be controlled by the turbulence perturbation upstream of the injector nozzle, hydrodynamic instabilities at the gas-liquid interface, and shear stresses between the liquid core and periphery of the jet.

KEYWORDS: Integrated CFD, Atomization, Multiphase flow, Nozzle flow, Spray

1. Introduction

Fuel injection is essential for the operation and performance of internal combustion (IC) engines. High pressure fuel injectors are used in both diesel and direct gasoline injection (DGI) engines. CFD (Computational Fluid Dynamics) combined with experiments has proved to be a useful tool to test many configurations in a short time, to test different injectors, as well as to vary operational parameters, such as injector positions, injection timing, duration, etc. For IC engines (both fuel and diesel), control of exhaust emission (such as unburned hydrocarbons and NO_x) and engine efficiency depends directly on the atomization of the liquid jet inside the combustion chamber (direct injection) or inside the admission pipe (indirect injection). Fundamental research on atomization and multi-phase processes in nozzle flow is multi-disciplinary in the sense that it involves the disciplines of fluid mechanics, multi-phase systems, measuring techniques and modeling [1–3]. Therefore, precise investigation of the mechanism of the primary breakup process, including that in the upstream region, is required because that mechanism controls both the length and the evolution of the potential core region (liquid core region where the magnitude of velocity is not damped toward the central axis) of the spray as well as generating all the characteristics of the dispersed region (droplet size, spray angle, etc.) [4–8]. The rate of primary atomization controls the mass fraction of the perturbed liquid fragments ejected from the core region.

In recent studies on the atomization mechanism in injector nozzles, no significant results of the effect of the upstream condition on the liquid breakup phenomenon have been obtained. In the present study, we mainly focused on the breakup process of the liquid column, formation of liquid film, and formation of small droplets in a high-speed turbulent cylindrical nozzle flow. The computational domain and rectangular structed mesh is created in reference to an actual injector nozzle used in diesel engines. Utilizing the governing equations for high-speed spray nozzle flow based on the LES-VOF model, an integrated simulation is performed to clarify the detailed consecutive atomization process and to clarify the characteristics of atomized droplets-gas two-phase flow.

2. Governing Equations

The numerical model represents the simultaneous unsteady flow of two immiscible, incompressible fluids, each having a constant viscosity and including surface tension. The flow is considered to be a laminar incompressible Newtonian and isothermal flow, which is governed by Navier–Stokes equations and continuity equations. The numerical simulation of atomizing flows composed of two immiscible fluids involves two coupled tasks: 1) resolving the flow field and 2) updating the position of the interface. The first task is completed by solving the Navier–Stokes equations taking into account the effect of the subgrid scale atomizing flow field by LES [9, 10]. The second task is performed using the Volume of Fluid (VOF) method [11–13]. The VOF method actually keeps and updates the field of

volume fraction of one fluid in each cell instead of the existence of the fluid at the surface location. The advantage of the VOF method is that there are no topological constraints. Thus, the VOF method has been widely used to track the interface of two immiscible fluids, such as water and air. The surface tension is taken into account through the Continuum Surface Force (CSF) model [14], where the surface force is transformed to a body force which is only non-zero in the interface region of limited thickness. The scalar F is used to denote the volume fraction field, also called the VOF field. Therefore, the governing equations for the one-fluid VOF-CSF model include the Navier–Stokes equations, a continuity equation and a VOF advection equation. This model comprises a single set of conservation equations for the whole flow field even though fluid properties are discontinuous across the fluid boundaries. These equations are written as follows.

The mass conservation equation:

$$\nabla \cdot \boldsymbol{v} = 0, \tag{1}$$

Momentum equation:

$$\frac{\partial}{\partial t}(\rho \boldsymbol{v}) + \nabla \cdot (\rho \boldsymbol{v}\boldsymbol{v}) = -\nabla p + \nabla \cdot \boldsymbol{\tau} + \int_{S(t)} \sigma \kappa' \boldsymbol{n}' \delta(\boldsymbol{x} - \boldsymbol{x}')\, dS, \tag{2}$$

When the interface is advected by the flow, the evolution of the VOF advection function is given by

$$\frac{\partial F}{\partial t} + \nabla \cdot (F\boldsymbol{v}) = 0, \tag{3}$$

where $\boldsymbol{v}$ is the velocity, ρ is the density, σ is the surface tension coefficient, κ is the curvature of the liquid surface and $\boldsymbol{\tau}$ is the viscous stress tensor. Also, $\boldsymbol{n}$ represents a unit vector normal to the liquid surface. The last term on the right hand side of Eq. (2) represents the source of momentum due to surface tension. It acts only at the interface (represented by the Dirac function $\delta(\boldsymbol{x})$) over the entire surface described by $S(t)$. The interface between the phases is simultaneously computed using a surface capturing methodology which employs the volume fraction of one of the phases (here taken to be the liquid) as an indicator function to identify the different fluids. The interface is not defined as a sharp boundary and a transition region exists where the fluid is treated as a mixture of the two fluids on each side of the interface, which would in reality be a discontinuous step. The indicator function, which is equivalent to the liquid-phase volume fraction F, is defined as

$$F = \begin{cases} 0 & \text{for a cell inside the gas} \\ 0 < F < 1 & \text{for a cell in the transitional region} \\ 1 & \text{for a cell completely in the liquid} \end{cases}$$

The VOF advection in Eq. (3) appears in the conservative form adopted from Puckett *et al.* [13] According to the definition of the indicator function F, the local density ρ and the local viscosity μ of the fluid are typically interpolated across the interface as follows:

$$\begin{cases} \rho = F\rho_l + (1 - F)\rho_g \\ \mu = F\mu_l + (1 - F)\mu_g, \end{cases} \tag{4}$$

where the subscripts l and g denote the liquid- and gas-phases, respectively. Since the interface is treated as a transitional zone, its exact shape and location are not explicitly known. During the numerical solution process, we apply the free-surface boundary conditions. There are three hydrodynamic boundary conditions at free surfaces: normal stress balance, tangential stress balance, and the kinematic equation. The kinematic condition is implied by the VOF advection. The surface integral in Eq. (2) that represents the surface tension, therefore, cannot be calculated directly. Brackbill *et al.* [14] overcame this problem with their continuum surface force (CSF) model, which represents the surface tension effects as a continuous volumetric force acting within the transition region.

The stress balance of dynamics is realized through the CSF model incorporated in the momentum equations by introducing a body force $\boldsymbol{F}_{sv}$. The surface tension can be modeled numerically as a body force, $\boldsymbol{F}_{sv}$, concentrated at the interface. The localized body force $\boldsymbol{F}_{sv}$ near the interface is calculated from the volume fraction data and is given by

$$\boldsymbol{F}_{sv} = \int_{s(t)} \sigma \kappa' \boldsymbol{n}' \delta(\boldsymbol{x} - \boldsymbol{x}')\, dS \approx \sigma \kappa \nabla F, \tag{5}$$

where κ is the curvature of the surface. The interface characteristic parameters, the normal to the interface $\boldsymbol{n}$ and curvature κ, are calculated as

$$\boldsymbol{n} = -\nabla F, \quad \widehat{\boldsymbol{n}} = \frac{\boldsymbol{n}}{|\boldsymbol{n}|} \tag{6}$$

$$\kappa = \nabla \cdot \widehat{\boldsymbol{n}} \tag{7}$$

The body force term of $\boldsymbol{F}_{sv}$ in r.h.s. in momentum Eq. (2) effectively removes the explicit boundary condition at the interface in the governing equations. The LES-VOF equations are derived from Eq. (2) through a localized volume averaging of the phase weighted properties. This process is more commonly known as filtering because it removes the very small scales of motion from direct calculation. This averaging in conjunction with the non-linear convection term in Eq. (2) produces an additional quantity into the momentum equation that cannot be directly calculated. The effect of the subgrid scales on the resolved eddies in momentum Eq. (2) is presented by the SGS stress. It is known as subgrid scale (SGS) stress since it represents the effect of the unresolved small scales of turbulence; it is given by

$$\boldsymbol{\tau}^{\mathrm{sgs}} = \overline{\boldsymbol{v}\boldsymbol{v}} - \overline{\boldsymbol{v}}\ \overline{\boldsymbol{v}} \tag{8}$$

The SGS stress is approximated through a single subgrid scale model of the eddy viscosity type that can be written as

$$\boldsymbol{\tau}^{\mathrm{sgs}} - \frac{2}{3}k\boldsymbol{I} = -\frac{\mu^{\mathrm{sgs}}}{\rho}(\nabla\overline{\boldsymbol{v}} + \nabla\overline{\boldsymbol{v}}^{T}), \tag{9}$$

where k is the subgrid scale turbulent energy and μ^{sgs} is the subgrid scale viscosity, both of which are calculated from the one-equation SGS turbulent energy transport model:

$$\begin{aligned}\frac{\partial k}{\partial t} + \nabla\cdot(k\overline{\boldsymbol{v}}) = \nabla\cdot[(\nu + \nu^{\mathrm{sgs}})\nabla k + \boldsymbol{\tau}^{\mathrm{sgs}}\cdot\overline{\boldsymbol{v}}] \\ -\epsilon - \frac{1}{2}\boldsymbol{\tau}^{\mathrm{sgs}} : (\nabla\overline{\boldsymbol{v}} + \nabla\overline{\boldsymbol{v}}^{T})\end{aligned} \tag{10}$$

$$\begin{cases}\epsilon = C_{\epsilon}k^{3/2}/\Delta \\ \nu^{\mathrm{sgs}} = C_{k}k^{1/2}/\Delta,\end{cases} \tag{11}$$

where (ϵ) is the SGS turbulent dissipation and (Δ) is the SGS length scale corresponding to the filter width (in most cases equivalent to the cell size). The filter width Δ is defined as $\Delta = (\Delta_x\Delta_y\Delta_z)^{1/3}$, where Δ_x, Δ_y, Δ_z are the grid spacings in the x, y and z directions, respectively. The constants, found from statistical considerations, are ($C_k = 0.07$) and ($C_{\epsilon} = 1.05$). Additional "subgrid" terms are produced by the filtering of the integral in Eq. (2) and the convection term in Eq. (3). The former represents the subgrid-scale influence of surface tension, known as the capillary force, and becomes important relative to the resolved surface tension when the surface curvature approaches the grid size. In cases where the influence of surface tension is small compared to that of inertia, the effect of subgrid-scale surface tension also becomes small. The latter term represents deformation of the liquid-gas interface due to subgrid-scale turbulence and is experienced at the grid scale as an added inter-phase diffusion. This effect is in direct opposition to the estimated SGS surface tension force. Numerical effort has been made to preserve the sharpness of the gas-liquid interface. Both these SGS terms, which can be potentially used to construct a new model for closure, have not been developed to date. Taking this into account, in the present numerical condition of ($\mathrm{We} \gg 1$), it is found that the influence of surface tension is relatively small compared with the effect of inertia at the resolved scales. The relatively fine mesh spacing (which minimizes SGS contributions) and the effect of grid-scale deformation of the liquid-gas interface tend to oppose one another.

3. Computational Method

Figure 1 depicts the major computational system expected in the present calculation. The present simulations focus on the region just downstream of a 0.2-mm-diameter nozzle by which a fully-developed turbulent liquid flow at a mean inlet velocity of $v_{l(\mathrm{in})} = 50\,\mathrm{m/s}$ is ejected into a dense, initially stationary gas. A constant velocity profile is applied to the inlet section and a convective outflow condition is applied to the outlet section. The nonslip condition for prescribed velocity is applied to the wall of inflow section and nozzle throat section. A free-slip condition for the prescribed velocity is applied to the surrounding wall outlet domain of the nozzle throat.

For the computational grid, the total number of cells is 1.8 million (Radial (r) × Azimuth (θ) × Axial (z) = 40 × 120 × 375 cells). The minimum cell resolution is 5 μm/cell. The working fluid of liquid-phase is assumed to be diesel fuel and the gas-phase is assumed to be air at a high pressure of 5.2 MPa and a high temperature of approximately 900 K, resulting in a liquid-gas density ratio of 42, as summarized in Table 1.

Also, the non-dimensional Reynolds, Mach and Weber numbers clearly indicate that the injected flow is turbulent and subsonic and is in the so-called atomization regime, in which surface tension and viscous forces are likely only to be important at small scale. These conditions are in many respects reasonably representative of those in contemporary large direct-injection diesel engines used in large vehicles. Compressibility, the effects of which are revealed at a Mach number of around 0.75, are also neglected in this instance because of methodological limitations. It is thought that the exclusion of compressibility effects accelerates perturbation growth rates on the liquid surface, but not to an extent that would invalidate our results.

Equations (1) and (2) are solved using the OpenFOAM finite volume CFD code [15], which employs spatial and temporal discretization schemes which are globally second-order accurate, but preserve the proper limits on physically-

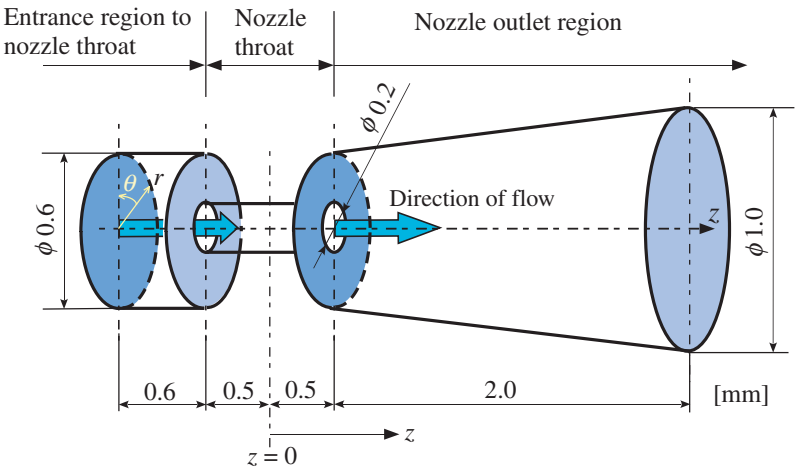

(a) Geometry of the computational domain

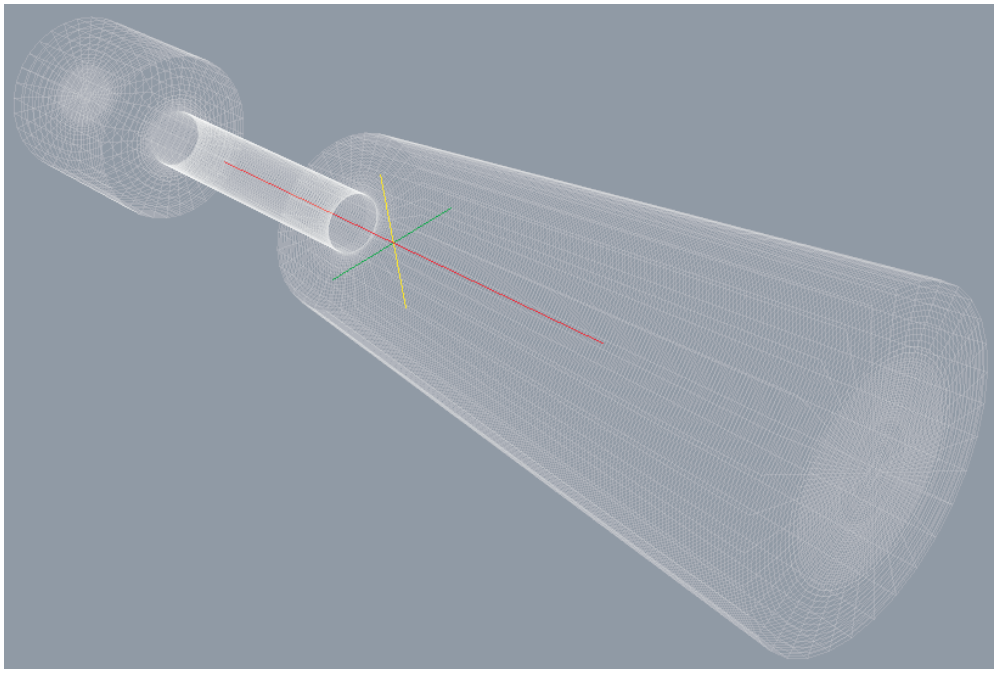

(b) Employed computational mesh

Fig. 1. Computational system for cylindrical nozzle.

Table 1. Numerical conditions.

Liquid-phase density	ρ_l	840.0	kg/m^3
Gas-phase density	ρ_g	20	kg/m^3
Inlet velocity	$v_{l(\mathrm{in})}$	50	m/s
Nozzle throat diameter	d	0.2	mm
Liquid-phase kinematic viscosity	ν_l	6.0×10^{-6}	m^2/s
Gas-phase kinematic viscosity	ν_g	8.5×10^{-7}	m^2/s
Surface tension	σ_l	0.0261	N/m

bounded variables. In the case of the convection term in the phase fraction transport Eq. (3), this is achieved through a flux limiting scheme and a conditional blending scheme where the solution might become unbounded. The numerical procedure for phase fraction transport Eq. (3) is based on the CICSAM differencing scheme proposed by Ubbink and Issa [16]. Recently, Ubbink [16] proposed a compressive bounded high-resolution scheme, termed the compressive interface capturing scheme for arbitrary meshes (CICSAM) based on the normalized variable diagram (NVD) [17], to deal with contact discontinuities such as fluid interfaces.

The CICSAM applies the NVD to ensure the boundness in approximating the face volume fluxes and switches

between two different high-resolution schemes to insure the sharpness of the interface. An outline of the CICSAM is given below to facilitate understanding of its theoretical background. The CISCAM scheme was formulated based on the idea of the donor-acceptor formulation, *i.e.*, as a scheme that varies as a function of the interface-cell face angle. The discretization depends on the interface velocity direction and the angle it makes with the integration cell face. However, rather than choosing as base schemes the downwind and upwind scheme, it utilizes the Hyper-C scheme and ULTIMATE-QUICKEST scheme of Leonard [17], the first being used when the cell face is directed perpendicular to the interface normal vector, and the later being used when the face normal vector is aligned with the normal to the interface.

The normalised variable of F forms the basis on which the high resolution schemes are constructed and is defined as [17]

$$\widehat{F} = \frac{F - F_U}{F_A - F_U}, \tag{12}$$

where the subscript D denotes the donor cell, A denotes the acceptor cell and U the upwind cell. The upper bound of the convection boundness criterion (CBC) described in Eq. (13) is the most compressive differencing scheme because it converts all gentle gradients into sharp steps, as indicated by Leonard and termed Hyper-C [17].

$$\widehat{F}_{f(\mathrm{CBC})} = \begin{cases} \min\left\{1,\ \dfrac{\widehat{F}_D}{c}\right\} & \text{for } 0 \le \widehat{F}_D \le 1 \\ \widehat{F}_D & \text{for } \widehat{F}_D < 0 \text{ or } \widehat{F}_D > 1, \end{cases} \tag{13}$$

where c is the Courant number of the donor cell. Such a characteristic is desired in the current modeling of moving interface problems. However, it is unstable due to its tendency to wrinkle the interface when the orientation of interface is normal to the flow direction. To overcome this problem, the ULTIMATE-QUICKEST (UQ) [17] described below is adopted in the CICSAM to continue the calculation where the Hyper-C is inadequate.

$$\widehat{F}_{f(\mathrm{UQ})} = \begin{cases} \min\left\{\dfrac{8c\widehat{F}_D + (1-c)(6\widehat{F}_D + 3)}{8},\ \widehat{F}_{f\mathrm{CBC}}\right\} & \text{for } 0 \le \widehat{F}_D \le 1 \\ \widehat{F}_D & \text{for } \widehat{F}_D < 0 \text{ or } \widehat{F}_D > 1 \end{cases} \tag{14}$$

The UQ is a high-resolution differencing scheme but it is still too diffusive to apply anywhere in the calculation of moving interface problems. Consequently, depending upon the orientation of the interface, the CISCAM applies a weighting factor $0 \ge \gamma_f \ge 1$ to smoothly switch between these two methods:

$$\widehat{F}_{f(\mathrm{CICSAM})} = \gamma_f \widehat{F}_{f(\mathrm{CBC})} + (1 - \gamma_f)\widehat{F}_{f(\mathrm{UQ})}, \tag{15}$$

where γ_l is related to the angle between the interface orientation and flow direction [16]. The fractional volume function on the cell face can then be obtained by rearranging Eq. (15) according to Equation (12). Furthermore, the solution procedure employs the implicit PISO algorithm in conjunction with conjugate gradient methods.

4. Results and Discussion

Figure 2 shows the instantaneous iso-surface of the liquid-phase volume fraction with velocity magnitude. Figure 3 shows the characteristics of the potential core of the liquid-phase jet flow just downstream of the nozzle aperture outlet. The potential core is represented by the superimposed results of the maximum liquid phase volume fraction ($F = 1$) in all computational time steps (500 time steps). Namely, this figure is obtained by superposing the calculation result in each time step with total time steps. The contours of instantaneous velocity magnitude in Fig. 3 are depicted in an streamwise plane extending from inside of the inflow duct to the initial diameters of the jet. Figure 4 shows the instantaneous vector and magnitude of velocity scalar profiles of the atomizing flow. The liquid-phase volume fraction is perturbed in the process of liquid-phase flow until the aperture inlet portion of the injector nozzle. The cylindrical inflow of liquid column is transformed to a small wavy liquid film downstream of the aperture exit due to the small vortex induced by the wake passing through the nozzle throat, which is due to the effects of the nozzle atomized turbulence and negative pressure gradient. When the magnitude of the perturbation amplitude for wavy liquid film is above a certain value, due to turbulent generation resulting from the boundary layer separation at the nozzle throat, the liquid film in the nozzle downstream is stretched to form ligaments. After that, the ligaments break up and subsequently form liquid droplets. Accordingly, the primary and the sequential process of the atomization mechanism in the injector nozzle, especially in the case of cylindrical fluid flow, is obtained by the present numerical method.

These phenomena clearly show the initial development of waves on the surface of the liquid column jet and their subsequent rapid growth due to the Kelvin-Helmholtz (K-H) instability caused by the sufficient velocity difference (large slip ratio) across the interface between gas and liquid-phases, leading to breakup into liquid ligaments, liquid film and droplets until it completely disintegrates. The salient characteristic feature is that the faster wave growth mode

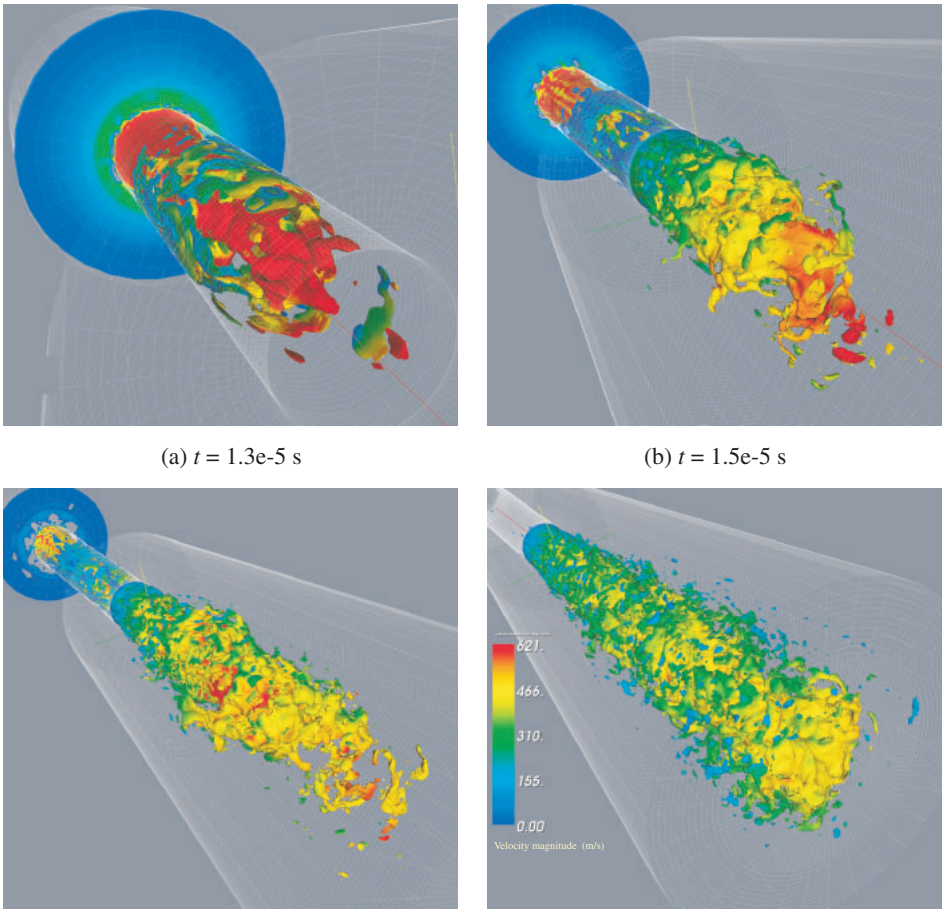

(a) t = 1.3e-5 s (b) t = 1.5e-5 s

(c) t = 1.7e-5 s (d) t = 3.0e-5 s

Fig. 2. Instantaneous iso-surface of liquid-phase volume fraction ($F = 0.5$) with velocity scalar magnitude.

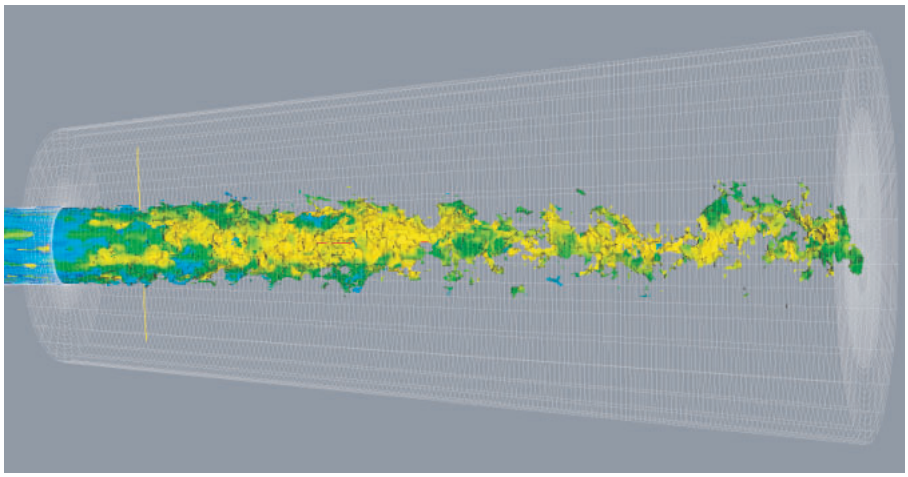

Fig. 3. Potential core of liquid-phase jet flow just downstream of the nozzle aperture outlet as represented by the superimposed results of maximum liquid phase volume fraction ($F = 1$) in all computational timesteps.

plays a key role in the enhancement of rapid breakup. These figures also show that the breakup process has strong three-dimensionality, even very close to the nozzle outlet. In the present computational system, as the interfacial gas-liquid velocity difference is large, it is considered that the most dominant factor of the primary interfacial instability generation is caused by Kelvin-Helmholtz (K-H) instability. Furthermore, there is a possibility that the instability mode of the small wave length which originates from the capillary waves influences the atomization of small droplets. However, such an instability mode caused by the capillary waves based on the surface tension force is not clear in the present study. As the magnitude of the length of the potential core (atomization length) obtained by the present

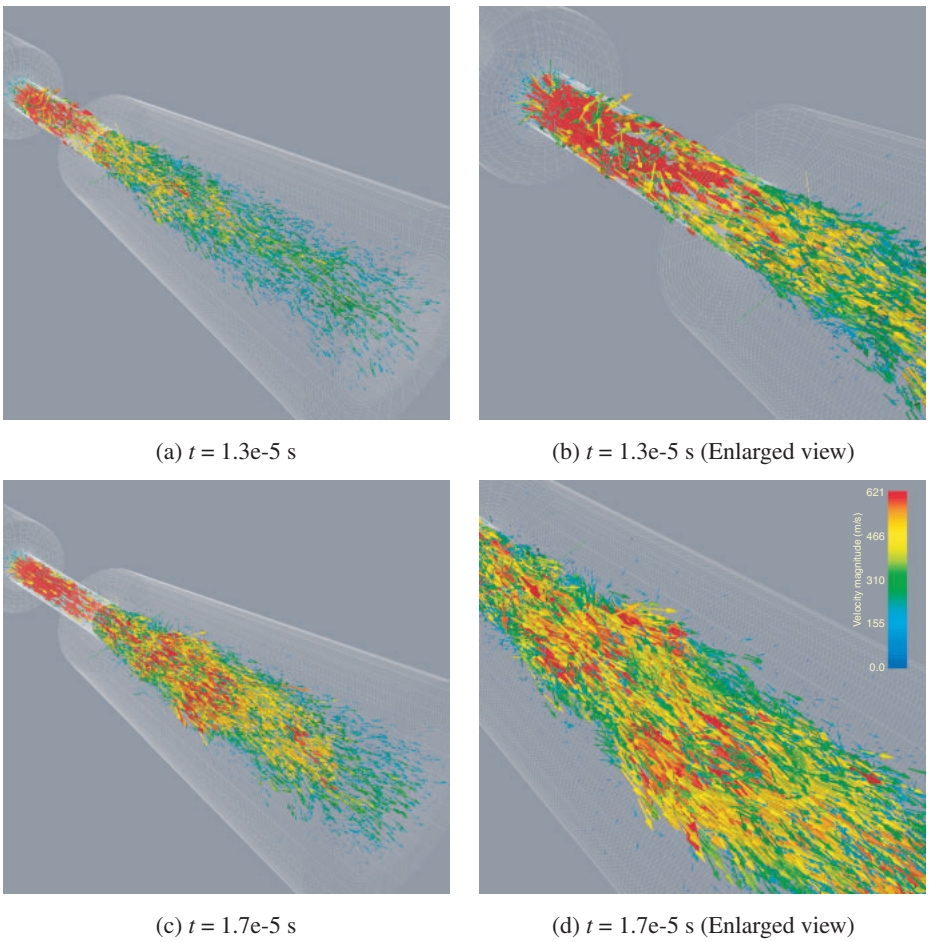

(a) t = 1.3e-5 s (b) t = 1.3e-5 s (Enlarged view)

(c) t = 1.7e-5 s (d) t = 1.7e-5 s (Enlarged view)

Fig. 4. Instantaneous velocity vector and magnitude of velocity profiles.

calculation exists in the turbulent jet region of the breakup regime map which is given by the measurement of Wu [18], it is supposed that proper numerical calculation is performed by our method.

According to Figs. 2 to 4, due to the developed liquid-phase flow acceleration in the entrance duct connected to the nozzle inlet aperture, large turbulent perturbations with the development of the recirculation flow are induced in the nozzle outlet section. Large scale vortices simulate the inner turbulence and small scale vortices simulate the micro-turbulence within the boundary layer of the liquid jet flow. The continuous growth of the circumferential surface perturbations can be clearly seen. This growth continues until the potential core consists only of a liquid-phase fraction connected by ligaments, which eventually rupture, completing its disintegration. As the velocity in the center of the liquid column is greater than that at the speed at the column periphery, the vortices tend to approach the liquid-gas interface. Also, the hydrodynamic shear stress between the liquid core region and the liquid periphery region becomes large because of an increase in the sharp velocity gradient in those regions. The combined effect of both those vortices initiates a Kelvin-Helmholtz (K-H) instability at the interface. The growth of the most unstable waves is controlled by the hydrodynamic shear stresses and which results in liquid ligaments form at the crest of each wave. Stretched by vortices in the gas phase, those ligaments break up into droplets. Enhancement of the breakup phenomena is caused by the implementation of turbulent nozzle entry conditions in our two-phase immiscible code. It can be noticed that the perturbation begins after 4.0 microseconds, which is the time it takes for the tip of the potential core to migrate to an aperture diameter of about 5.0. A spray angle of 25.29° is also obtained. It is found that the length of the potential core of the cylindrical atomizing nozzle flow almost agrees with the general axisymmetric nozzle flow such as that by Reitz's analysis, namely, an aperture diameter of 3 to 7 distance [4, 5]. The initial perturbations of the liquid column surface resulting from initial wave growth are due to a combination of nozzle-generated turbulence and relaxation of the velocity profile as the liquid exits from the aperture.

The backward flow with flow separation and recirculation flow is found in the vicinity of the gas-liquid interface of wavy liquid films close to the wall of the nozzle exit section. The recirculation flow enhances the growth of the interfacial instability and of the liquid film wave perturbation. It consecutively enhances the breakup of elongated liquid ligaments and the separation of droplets. Therefore, the recirculation flow in the gas-liquid interfacial region may possibly be regarded as the main factor which induces the inception of the liquid jet atomization process.

Figure 5 shows the resolved magnitude of turbulent energy k profiles just downstream of the nozzle aperture outlet.

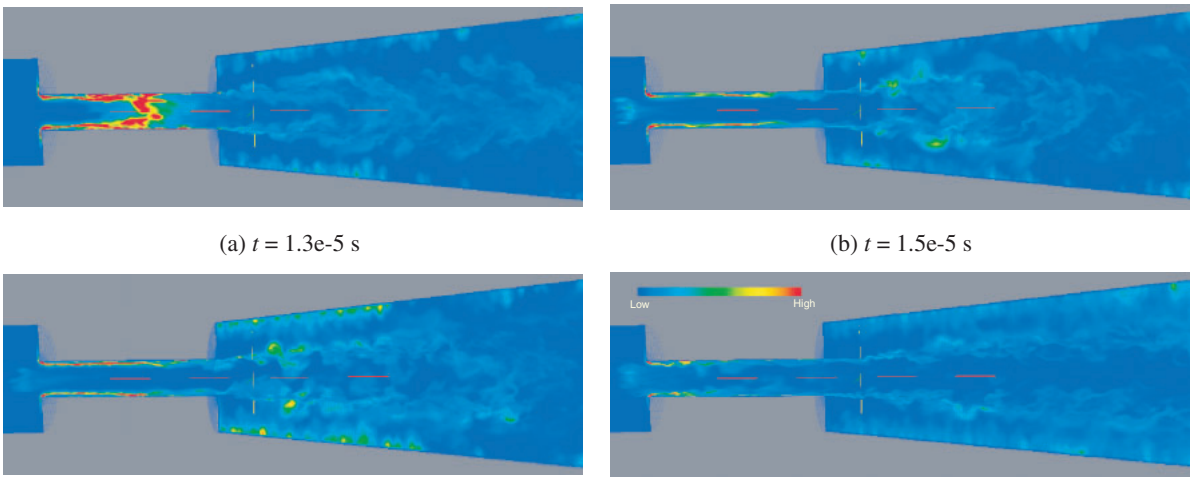

(a) t = 1.3e-5 s (b) t = 1.5e-5 s

(c) t = 1.7e-5 s (d) t =3.0e-5 s

Fig. 5. Magnitude of instantaneous turbulent energy k profiles.

According to Fig. 5, although there are some irregularities due to the relatively short sampling time, there is clear evidence that much higher turbulent energy is produced in the nozzle throat region as well as around the gas-liquid interface of wavy liquid films and separated droplets. Because two-phase turbulent energy develops in the nozzle throat region, the separation of the small droplets from the perturbed liquid film with subsequent K-H instability is enhanced by the growth of the amplitude of the wavy liquid film. The fully-developed cylindrical liquid-phase flow produced by the inflow duct leading to the entrance of the nozzle aperture shows a characteristic high-velocity core, with relatively large-scale irregularities resulting from the turbulent eddies and unsteady flow separation generated within the boundary layers in the inflow duct, which are a source of initial liquid jet surface perturbation. It is found that these bigger initial disturbances affecting the jet surface enhance the rapid atomization which is closely related to the importance of nozzle-generated turbulence.

The evolution of droplet diameter is basically dominated by the local scale of relative-velocity fluctuations between the gas- and liquid-phases. In this manner, LES plays a key role in providing accurate local estimation of the gas-phase turbulent statistical quantities.

Figure 7 shows the statistical result for frequency of droplet diameter distribution f_D as a function of streamwise coordinate z and droplet diameter D_p in all integrated time steps. The statistical method for analyzing the frequency of the droplet diameter profile is described as follows. By dividing the computational domain into 50 sections in the streamwise direction (z-direction), droplet-size distributions during the statistical time at each cross-section can be obtained (See Fig. 6). A rectangular parallelepiped with a certain thin thickness is assumed to be the control section. When the central point of a certain liquid droplet is located in the internal parallelepiped, this droplet is regarded as a droplet which exists in that cross section. The diameter distribution of the atomizing droplets is calculated in an arbitrary position in the thin cross-sectional computational region that was perpendicular to the z-axis having a certain thickness. Each droplet diameter is calculated from droplet volume obtained by taking into account the volume fraction occupying the computational meshes and also taking the mesh size into account. In the process of diameter profile calculation, the shape of each liquid droplet is assumed to be spherical. If the droplet fraction occupies part of the grid, the ratio of the fractional volume to the grid volume is computed. The droplet fraction is extracted and the equivalent fractional droplet diameter is defined as the diameter of a sphere having the same volume as the fractional droplet, which is regarded as a sphere whose volume is constant (See Fig. 6). When the droplet diameter in the n-th section is designated as D_{pn}, the frequency of the droplet diameter profiles in the range of $(D_{pn} - 1)$ to D_{pn} in the cross section is obtained in all the statistical times.

The frequency f_D is analyzed from the iso-surface data of the liquid-phase volume fraction ($F = 0.5$). The distribution of the atomizing droplet diameter is calculated in arbitrary positions in the thin cross-sectional computational region that was perpendicular to the z-axis having a certain thickness. The ordinate denotes the droplet diameter distribution frequency f_D, and the abscissa denotes the droplet diameter D_p. It is found that the peak value of f_D shifts the droplets diameter D_p tending to become large with z. On the other hand, the magnitude of peak frequency decreasing with an increase in streamwise coordinate z. In other words, atomization of the homogeneous droplets of relatively large size is enhanced as the cross-sectional region approaches the vicinity of the outlet domain. The main reason for this phenomenon is that the coalescence of the small droplets occurs with the homogeneous atomization downstream of the nozzle throat.

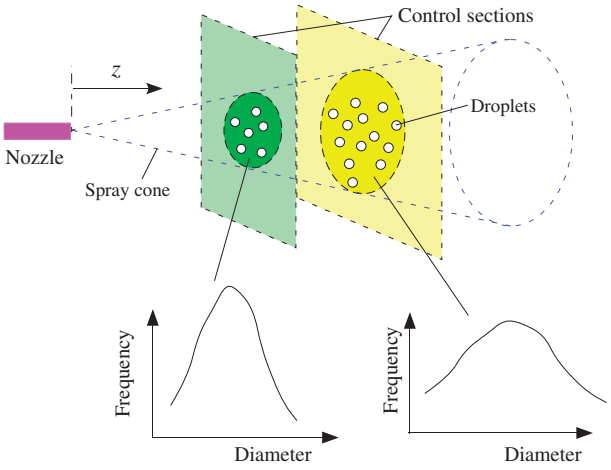

(a) Statistical analysis of droplet diameter profiles

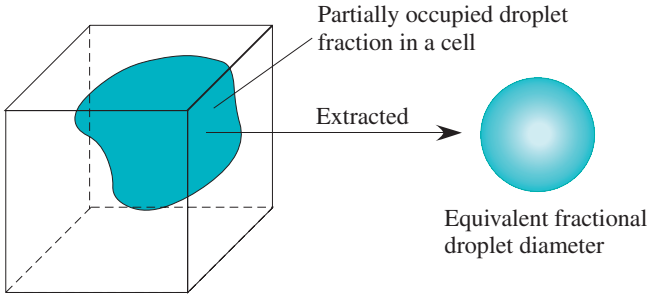

(b) Treatment of subgrid scale size of droplet diameter

Fig. 6. Schematic of the statistical analysis of frequency of droplet diameter profile.

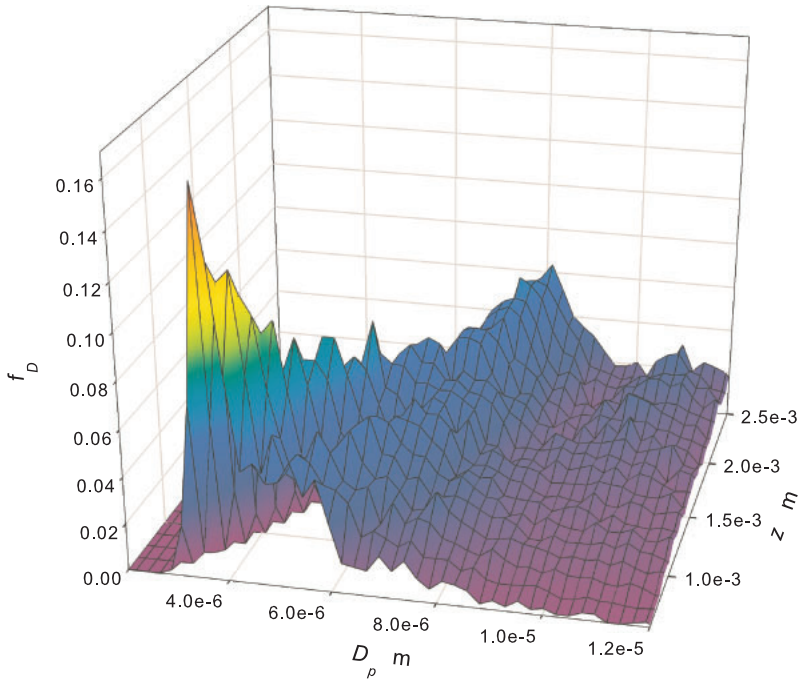

Fig. 7. Statistical result for frequency of droplet diameter distribution f_D as a function of streamwise coordinate z and droplet diameter D_p in all integrated time steps. f_D is analyzed from the iso-surface data of the liquid-phase volume fraction ($F = 0.5$).

5. Conclusions

The primary and the sequential process of the atomization mechanism in the injector nozzle, especially in the case of cylindrical liquid nozzle flow, was obtained by the present integrated numerical method.

1. In the initial perturbations of the liquid column surface, the initial wave growth was characterized by a combination of cylindrical nozzle-generated turbulence and relaxation of the velocity profile as the liquid exited from the aperture.
2. It was found that as the velocity in the center of the liquid column is greater than that of the speed at the column periphery, the vortices tend to approach the liquid-gas interface. It was also found that the hydrodynamic shear stress between the core region and the periphery region of the liquid column becomes large because of an increase in the sharp velocity gradient in those regions. The combined effect of both those vortices and share stress initiates a Kelvin-Helmholtz instability at the interface.
3. The initial development of waves on the surface of the liquid column jet and their subsequent rapid growth due to the Kelvin-Helmholtz instability causes the progressive atomization process which leads to the breakup into liquid ligaments, liquid film and droplets until it completely disintegrates.
4. A computational method for analyzing atomizing droplets diameter distribution was developed. It was found that the atomization of homogeneous droplets of relatively large size is enhanced as the cross-sectional region approaches the vicinity of the outlet domain. The main reason for this phenomenon is that the coalescence of the small droplet occurs with the homogeneous atomization downstream of the nozzle throat.

Acknowledgments

This research was supported by a Grant-in-Aid for Scientific Research (C. No. 17686015) from the Ministry of Education, Culture, Sports, Science and Technology, Japan, and also by TEPCO Research Foundation, Japan.

REFERENCES

[1] Faeth, G. M., Hsiang, L. P., and Wu, P. K., (1995), "Structure and breakup properties of sprays," *Int. J. Multiphase Flow*, **21**(1): 99–127.
[2] Sallam, K. A., Dai, Z., and Faeth, G. M., (2002), "Liquid breakup at the surface of turbulent round liquid jets in still gases," *Int. J. Multiphase Flow*, **28**(3): 427–449.
[3] Sallam, K. A., Dai, Z., and Faeth, G. M., (1999), "Drop formation at the surface of plane turbulent liquid jets in still gases," *Int. J. Multiphase Flow*, **25**: 1161–1180.
[4] Lin, S. P., (2003), *Breakup of liquid sheets and jets*, Cambridge University Press, New York, NY.
[5] Lin, S. P., and Reitz, R. D., (1998), "Drop and spray formation from a liquid jet," *Ann. Rev. Fluid Mech.*, **30**: 85–105.
[6] Zaleski, S., Li, J., and Succi, S., (1995), "Two-dimensional Navier–Stokes simulation of deformation and breakup of liquid patches," *Phys. Rev. Lett.*, **75**(2): 244–247.
[7] Leboissetier, A., and Zaleski, S., (2001), "Direct numerical simulation of the atomization of liquid jet," *Proceeding of the ILASS-Europe 2001, Zurich, 2–6, Sept. 2001*, (in CD–ROM).
[8] Villiers, D. E., (2004), "The potential of Large Eddy Simulation for the modeling of wall bounded flows," *Ph. D Thesis, Imperial College of Science, Technology and Medicine*.
[9] Apte, S. V., Gorokhovski, M., and Moin, P., (2003), "LES of atomizing spray with stochastic modeling of secondary breakup," *Int. J. Multiphase Flow*, **29**(9): 1503–1522.
[10] Vinkovic, I., Aguirre, C., Simoëns, S., and Gorokhovski, M., (2006), "Large eddy simulation of droplet dispersion for inhomogeneous turbulent wall flow," *Int. J. Multiphase Flow*, **32**(3): 344–364.
[11] Hirt, C. W., and Nichols, B. D., (1981), "Volume of fluid (VOF) method for the dynamics of free boundaries," *J. Comput. Phys.*, **39**(1): 201–225.
[12] Garbero, M., Vanni, M., and Fritsching, U., (2006), "Gas/surface heat transfer in spray deposition processes," *Int. J. Heat and Fluid Flow*, **27**(1): 105–122.
[13] Puckett, E. G., Almgren, A. S., Bell, J. B., Marcus, D. L., and Rider, W. J., (1997), "A high-order projection method for tracking fluid interfaces in variable density incompressible flows," *J. Comput. Phys.*, **130**(2): 269–282.
[14] Brackbill, J. U., Kothe, D. B., and Zemach, C., (1992), "A continuum method for modeling surface tension," *J. Comput. Phys.*, **100**: 335–354.
[15] OpenCFD. (http://www.opencfd.co.uk/).
[16] Ubbink, O., and Issa, R. I., (1999), "A method for capturing sharp fluid interfaces on arbitrary meshes," *J. Comput. Phys.*, **153**: 26–50.
[17] Leonard, B. P., (1991), "The ULTIMATE conservative difference scheme applied to unsteady one-dimensional advection," *Comput. Meth. Appl. Mech. Engrg.*, **88**(1): 17–74.
[18] Wu, P.-K., Miranda, R. F., and Faeth, G. M., (1995), "Effects of initial flow conditions on primary breakup of nonturbulent and turbulent round liquid jets," *Atomization and Sprays*, **5**(2): 175–196.